FIELD EXPERIMENTS IN SUPPORT OF EUROTRMM

Jacques Testud[1], Stéphane Oury[1], Erwan LeBouar[1], Tom Keenan[2] and Frank Marks[3]

[1] CETP, [2] BMRC, [3] NOAA/HRD

1. Introduction

In support to the EuroTRMM program the aim of the field experiments is two fold:

i) to provide some ground truth for the TRMM rain retrieval, and particularly for the rain retrieval derived from the space borne precipitation radar.

ii) to provide some local ground comparison data for the assimilation experiment of ECMWF.

This paper is based on two experiments :

a) Ground based : the Darwin C-band polarimetric radar. The Darwin radar is one of the primary validation site of TRMM and is surrounded by a dense rain gauge network and by several disdrometers;

b) Airborne dual beam Doppler : The NOAA-P3 equipped with an X band tail radar operated following the FAST (Forward and Aft scanning STrategy) scanning strategy, and with in situ microphysical data was deployed during CAMEX, a field experiment associated with TEFLUN, aiming to provide a physical insight of precipitation systems observed by TRMM.

Thus this paper is centred on two objectives:

To carefully analyse data from TRMM overpasses and provide high quality description of the rainfall rate fields at a scale comparable with that of the TRMM PR.

To provide a description, on the mesoscale, of the wind field and of the precipitation field associated to Hurricane Bonnie, and to investigate some comparison with the Hurricane produced by the assimilation experiment of ECMWF.

The topics addressed hereafter are the following:

1. the properties of the drop size distribution DSD and the inverse model for microwave remote sensing of the precipitation

2. the algorithms for rain rate retrieval for the TRMM precipitation radar, for the C-band polarimetric radar, and for the airborne dual beam radar;

3. the mesoscale features observed in Hurricane Bonnie and their comparison with the assimilation experiment of ECMWF.

2. DSD Model and Rain Relations

The quantitative estimate of rain from microwave remote sensing, active (weather radar) or passive (microwave radiometer), is subject to the natural variability of the raindrop size distribution (DSD). The first step in establishing « rain relations », (that is, relationships between parameters describing the bulk characteristics of the medium, and parameters describing the property of the medium - propagation, emissivity, scattering - at a probing frequency) is to be able to *characterise* the DSD. This is the reason for developing in the next section, the concept of *normalisation* of the DSD.

2.1. The concept of normalized DSD

2.1.1. *Theory*

The physical characterisation of any observed raindrop spectrum raises three questions:

(i) What "rain intensity" corresponds to this spectrum?

(ii) What is the "mean" drop diameter?

(iii) What is the "intrinsic" shape of the raindrop size distribution?

In order to characterise "rain intensity", two parameters may be considered: the liquid water content *LWC* (in g/m^3), or the rainfall rate *R* (in mm/h). Traditionally, *R* is more often adopted than *LWC*. However it may be argued that *LWC* is a better parameter than *R* since it has a clearer physical meaning (at altitude, *R* is subject to vertical air motion and change in terminal fall velocity related to air density). There is no ambiguity in the definition of *LWC*. It is simply proportional to the third moment of the dropsize distribution *N(D)* [*N*: number of particles per unit volume and per interval of diameter, in m^{-4}; and *D*: drop diameter in m]. More specifically:

$$LWC = \frac{\pi \rho_w}{6} \int_0^\infty N(D) D^3 dD \tag{1}$$

As the "mean" diameter, this paper uses the "volume weighted" mean diameter D_m [generally referred to as the "mean volume diameter"] defined as the ratio of the fourth to the third moments of the DSD:

$$D_m = \frac{\int_0^\infty N(D) D^4 dD}{\int_0^\infty N(D) D^3 dD} \tag{2}$$

D_m is in fact very close to the median volume diameter D_0 generally used by radar meteorologists (Ulbrich, 1983).

The definition of the "intrinsic" shape is intimately related to the concept of normalisation of raindrop spectra. Normalisation is interesting when it is intended to compare the shape of two spectra that have not the same liquid water content *LWC* and/or mean volume diameter D_m. Thus, normalisation should be defined in such a way that the "intrinsic shape" be independent of *LWC* and/or D_m. A general expression of the normalisation of the DSD is:

$$N(D) = N_0^* F(D / D_m) \tag{3}$$

where N_0^* is the scaling parameter for concentration, and D_m is the scaling for diameter.

$F(X)$ in (3) denotes the "normalised DSD" describing the "intrinsic" shape of the DSD (noting $X = D/D_m$). Testud et al. (2001) stated that, in order the normalised function F be independent of LWC and D_m, the N_0^* parameter should be proportional to LWC/D_m^4. More specifically, they recommended the following particular definition of N_0^*:

$$N_0^* = \frac{4^4}{\pi \rho_w} \frac{LWC}{D_m^4} \tag{4}$$

(ρ_w: density of liquid water)

The interest of (4) is that, for an exponential DSD as $N(D) = N_0 \exp(-\Lambda D)$, N_0^* verifies:

$$N_0^* = N_0 \tag{5}$$

This equality justifies the notation of parameter N_0^* and allows us to give a simple physical interpretation of it: *Whatever be the shape of an observed DSD, the corresponding N_0^* is the intercept parameter of the exponential DSD with the same LWC and D_m.* N_0^* is referred to in the following as the "*normalised intercept parameter*" of the DSD.

2.1.2. Shape of the DSD

The above defined normalisation has been applied to the following data sets:

(i) Airborne microphysical data collected by PMS probes on board the NCAR Electra during 21 flights in TOGA-COARE (West Equatorial Pacific, October 1992-February 1993).

(ii) 5 day record of a ground based disdrometer operated by BMRC (Bureau of Meteorology Research Centre) at Darwin.

(iii) Nine month record of a ground based disdrometer operated by ETH at Zurich.

Data sets (i) and (ii) are representative of tropical oceanic convection, while (iii) is representative of mid-latitude weather systems. The application of the normalisation to the TOGA-COARE data allowed to identify the "intrinsic" shape of the DSD. Four rain categories were considered: "stratiform", "convective <10mm/h", "convective 10 to 30 mm/h", and "convective >30mm/h". It was found in Testud et al. (2001) that the "normalised" shape of the DSD for the various categories are very close to one another, but departs significantly from the exponential. In particular the tail of the distribution was found definitely sub-exponential, similar to that obtained with a Gamma DSD with $\mu = 2$ to 4. However a Gamma DSD would underestimate the concentration of small drops with normalised diameter < 0.7. It is the reason to prefer the "modified exponential" (illustrated in Fig. 1) defined as:

$$N(D) = N_0^* \exp\left[a - 4\frac{D}{D_m} - s\sqrt{\left(\frac{D}{D_m} - X_0\right)^2 + b}\right] \tag{6}$$

with $s = 1.5$; $b = 0.06$; $X_0 = 1.124$; $a = 0.705$.

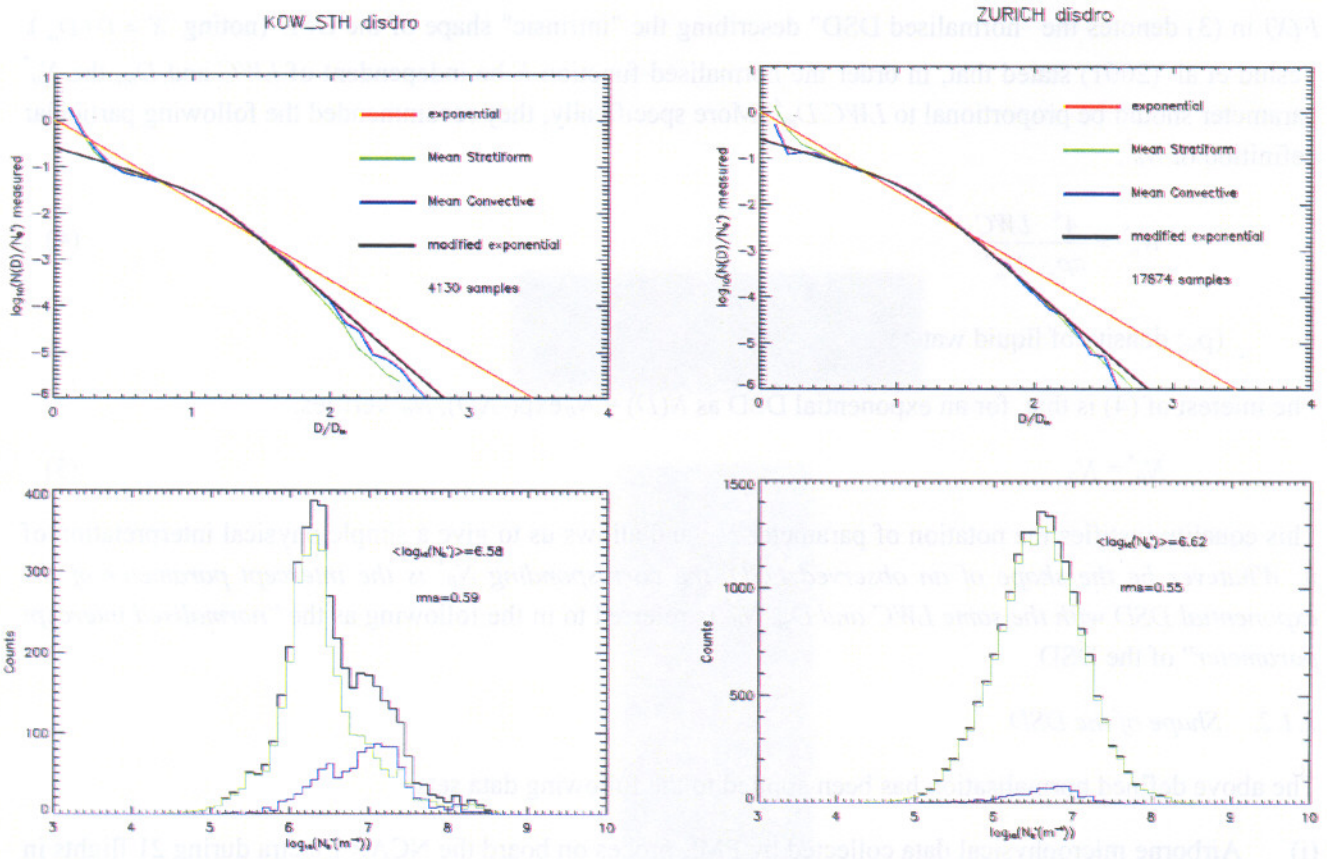

Fig 1: DSD statistics derived from ground based disdrometers. Left diagrams: 5 rainy days of January 1998 at Darwin (Australia). Right diagrams: 9 months of 1993 at Zurich (Switzerland). Upper diagrams: observed normalised shape of the DSD distinguishing the two rain categories stratiform or convective, compared with two theoretical shapes, exponential and "modified exponential. Lower diagrams: corresponding histograms of N_0^* for convective, stratiform and all together.

While the TOGA-COARE data is representative of a statistics at a typical altitude of 3 km above sea level, Fig.1 illustrates the DSD statistics obtained from the two ground based disdrometer of Darwin (Australia) and Zurich (Switzerland). It is striking that the intrinsic shape of the DSD is about the same at Darwin and Zurich, and is very close to the "modified" exponential adjusted to the TOGA-COARE data.

2.1.3. *Statistics of N_0^**

As opposed to the remarkable stability of the shape of the DSD whatever the rain type or climate, the N_O^* parameter is affected by a large variability, ad illustrated in Fig.1. The histogram of N_O^* observed at Darwin is very similar to that derived from TOGA-COARE (see Testud et al., 2001). It spreads over two decades and shows a bimodal shape, reflecting a distinct behaviour between stratiform and convective rain. Typical values of N_O^* in this climatic zone appear to be $2.2 \times 10^6 m^{-4}$ for stratiform rain and $2 \times 10^7 m^{-4}$ for convective. The histogram in Zurich also spreads over two decades, but appears mono modal and the distinction between the behaviour of stratiform and convective rain seems less marked. Thus the variability of the DSD according to rain type, rain intensity or climate appears essentially controlled by parameter N_0^*.

2.2. The inverse model for rain radar retrieval

2.2.1. Relationships between moments of the DSD

Moments of the DSD represent more or less faithfully most of the integral parameters of the DSD of interest in the "rain relations. For example, the liquid water content *LWC* is proportional to M_3; the rainfall rate R to $M_{3.67}$ [assuming that the terminal fall velocity is $V_t \propto D^{0.67}$]; the radar reflectivity Z to M_6 and the specific attenuation K to M_3 (the last one, under the Rayleigh approximation). A general expression of the ith order moment of the DSD is:

$$M_i = \int N_0^* F(D/D_m) D^i dD = N_0^* D_m^{i+1} \xi_i \tag{7}$$

where ξ_i is the ith order moment of the *normalised distribution F(X)*:

$$\xi_i = \int F(X) X^i dX \tag{8}$$

Thus, between two moments of order i and j, the following relationship stands:

$$\frac{M_i}{N_0^*} = \xi_i \xi_j^{-\left[\frac{i+1}{j+1}\right]} \left[\frac{M_j}{N_0^*}\right]^{\left[\frac{i+1}{j+1}\right]} \tag{9}$$

with N_0^* ranging typically between 10^6 and $10^8 m^{-4}$.

Equation (9) establishes that, *when normalised by* N_0^*, the relationship between two moments of order i and j of the DSD is a power-law whose exponent is $(i+1)/(j+1)$, *independent of the shape of the DSD.* Taking the particular instance of the *Z-R* relationship, as $Z = M_6$ and $R \propto M_{3.67}$ (with a power-law as $V_t \propto D^{0.67}$ for terminal fall velocity), (9) sets the exponent of the Z/N_0^*-R/N_0^* relationship to 7/4.67 = 1.499. Thus it may be written that:

$$Z/N_0^* = a\left[R/N_0^*\right]^{[1.499]} \quad \text{or} \quad Z = aN_0^{*[-0.499]} R^{1.5} \tag{10}$$

For R in mm/h, Z in $mm^6 m^{-3}$, N_0^* in m^{-4}, and with the terminal fall velocity law $V_t = 386.6D^{0.67}$ (V_t in m/s, D in m) [Atlas and Ulbrich, 1977], it is found that: $a = 5.2x10^4 \xi_6 \xi_{3.67}^{-1.499}$. For the modified exponential, ξ_6 = 0.034995 and $\xi_{3.67}$ = 0.023441.

Traditionally, empirical power-law *Z-R* relationships are established from a linear correlation between $\log_{10}(Z)$ and $\log_{10}(R)$ on a given data set. Each of them is specific of a particular rain type or climate. As opposed to the traditional *Z-R* relationship, (10) specifies a relationship randomised by N_0^*, and, as far as the normalised shape is stable, it represents a "universal" relationship which applies to *any* type of rain under *any* climate. Table 1 presents a test of validity of (10) based on a linear correlation analysis between $\log_{10}(Z/N_0^*)$ and $\log_{10}(R/N_0^*)$ applied to the full TOGA-COARE data set.

Empirically derived (full TOGA-COARE data set)	$Z/N_0^* = 4.73x10^{-5}\left[R/N_0^*\right]^{1.494}$ (with ρ^2=0.9888)
Theoretical (with Modified Exponential)	$Z/N_0^* = 4.87x10^{-5}\left[R/N_0^*\right]^{1.499}$

Table 1: The Z-R *relationships parameterised by* N_0^**, as determined empirically (from the TOGA-COARE data set) or theoretically (with, as shape function, the Modified Exponential)*

A quite good agreement is found between the "universal" relationship as well concerning the exponent of the power law as for the coefficient. The correlation coefficient is very close to 1 (ρ^2=0.9888) while it is only 0.838 with a standard *Z-R* relationship fitted to the same data.

2.2.2. *General model of the "rain relationships"*

Extensive variables (that is, variables proportional to particle concentration) like rainfall rate R, liquid water content LWC, equivalent radar reflectivity Z_e, specific attenuation A, specific differential phase shift K_{DP} are integral parameters of the DSD. Their general expression is:

$$P = \int f_P(D)N(D)dD \tag{11}$$

where P denotes the parameter in question and $f_P(D)$ the corresponding weight of an individual raindrop of diameter D. In the general case, $f_P(D)$ cannot be expressed as $\propto D^{\alpha}$, thus P is not proportional to a moment of the DSD. Nevertheless, introducing the representation of $N(D)$ by (3), (11) transforms as:

$$P = N_0^* D_m \int f_P(X.D_m)F(X)dX \tag{12}$$

Eq.(12) shows that , if the intrinsic shape is stable, P/N_0^* is a function of D_m *only*. Thus considering two parameters P_1 and P_2, by eliminating D_m between their two expressions given (12), we may establish a *functional* relationship between P_1/N_0^* and P_2/N_0^*.

The same reasoning stands with "intensive variables" (whose definition is independent of particle concentration) like the differential reflectivity Z_{DR} or the back-scattering phase shift δ, except that there is no need to normalise by N_0^*.

Fig.2 illustrates a few "rain relationships" useful for rainfall algorithm retrieval with a ground based C-band radar. The rain parameters are calculated for rain at 10°C temperature and horizontal incidence of the radar beam, using a T-matrix scattering model, and laws for particle terminal fall velocity and particle oblateness as defined in Le Bouar et al, (2001). Various shapes of the DSD are considered: Gamma distributions with shape parameter μ between –1 and +4, or "modified exponential". It can be seen that the various functional relationships are not very sensitive to the assumed shape. This, added to the fact that the actual shape of the DSD is observed very stable and close to the "modified exponential" confirms the solidity of the inverse model based on relationships parameterised by N_0^*. Note that most relationships are well represented by a power law.

3. Rain Rate Algorithm Retrieval

Weather radars considered in this paper operate at attenuated frequency. The TRMM precipitation radar operates near 14 GHz. With this radar, despite the near nadir operation that limits the path length through rain, the path integrated attenuation may reach in heavy rain may reach 10 to 20 dBZ (one way). The NOAA-P3 airborne Doppler tail radar operates at X-band (9.3 GHz). Its sampling strategy is "fore and aft" conical scanning, allowing one to observe any storm under two viewing angles. The practical range, limited by along path attenuation and cross beam resolution, is 40 to 50 km. The Darwin radar is a ground based C band polarimetric radar, moderately attenuated through rain. Nevertheless at long range (as 100 km) and through heavy rain, along path attenuation may reach 15 dBZ.

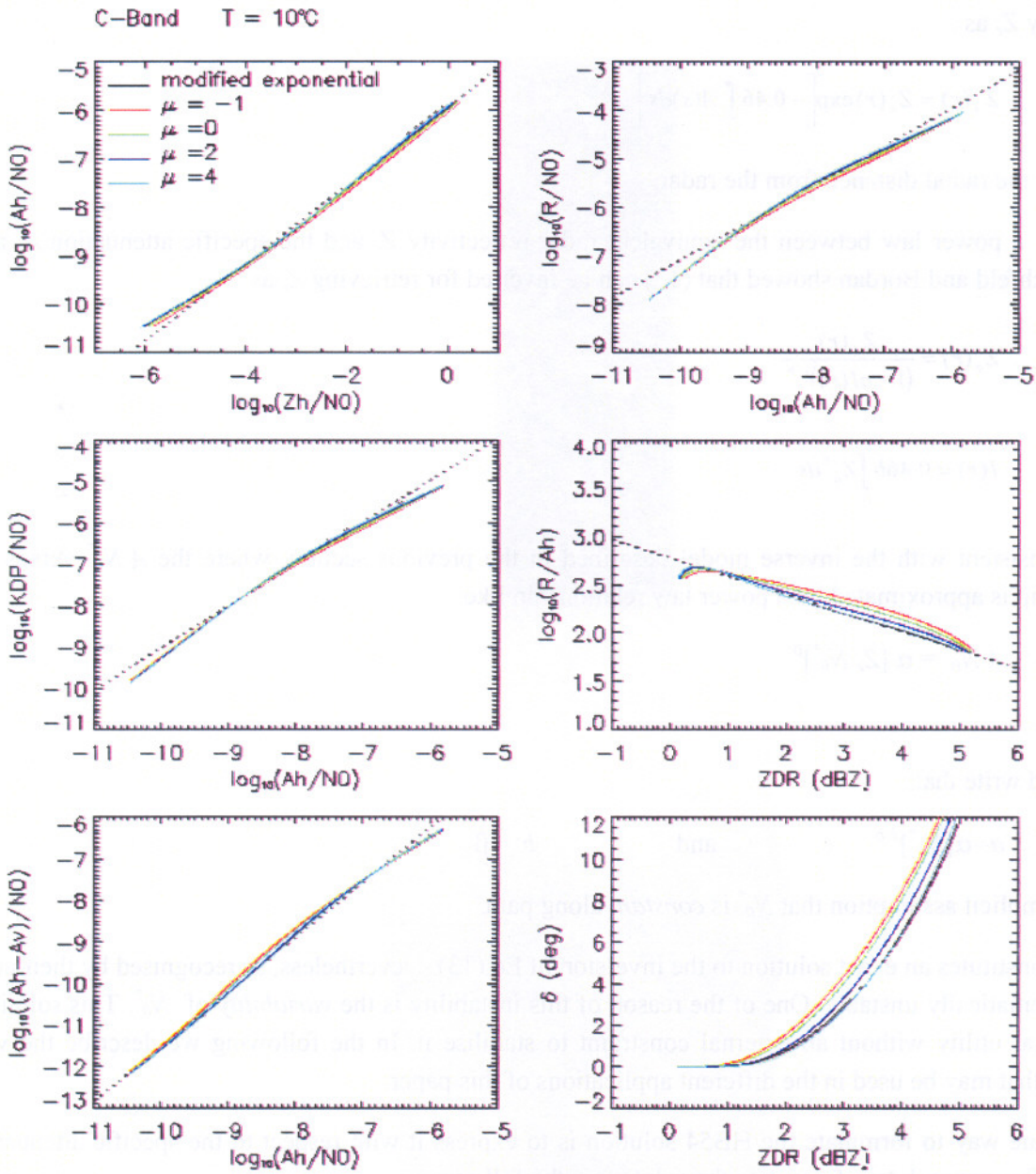

Fig.2 : *Inverse model for a C-band ground based radar. Left diagrams, from top to bottom: normalised specific attenuation A_H/N_0^* against normalised radar reflectivity Z_H/N_0^*; normalised specific differential phase shift K_{DP}/N_0^* against A_H/N_0^*; normalised specific differential attenuation $A_{DP}/N_0^* = (A_H-A_V)/N_0^*$ against A_H. Right diagrams, from top to bottom: normalised rain rate R/N_0^* against A_H/N_0^*; ratio R/A_H against Z_{DR}; Back-scattering differential phase shift δ against Z_{DR}. In each diagram, the dotted line represents the best power law fit to the functional relationship corresponding to the "modified exponential".*

The Darwin radar is a primary validation site of TRMM, while the NOAA-P3/42 was used during CAMEX, one of the major airborne validation experiment of TRMM. The object of this section is to present some kind of unified approach for rain rate algorithm retrieval for these three radars operating at attenuated frequency (TRMM-PR, NOAA-P3 tail radar and Darwin C-POL radar).

3.1. A general formulation

Most algorithms used in this paper belong to the class of « rain profiling » algorithms. These algorithms are derived from Hitchfeld and Bordan's (1954) formulation (referred to hereafter as HB54). With a classical radar, the primary radar observable is the « apparent » radar reflectivity Z_a related to the « true » equivalent reflectivity Z_e as :

$$Z_a(r) = Z_e(r)\exp\left[-0.46\int_0^r A(s)ds\right] \tag{13}$$

where r is the radial distance from the radar.

Assuming a power law between the equivalent radar reflectivity Z_e and the specific attenuation A, as $A = a.Z_e^{\,b}$, Hitchfeld and Bordan showed that (13) can be inverted for retrieving Z_e as:

$$Z_e(r) = \frac{Z_a(r)}{\left(1 - aI(r)\right)^{1/b}} \tag{14}$$

with $$I(r) = 0.46b\int_0^r Z_a^{\,b}\,ds \tag{15}$$

To be consistent with the inverse model described in the previous section, where the A/N_0^* versus Z_e/N_0^* relationship is approximated by a power law relationship like:

$$A/N_0^* = \alpha\,[Z_e/N_0^*]^{\beta} \tag{16}$$

We should write that:

$$a=\alpha[N_0^*]^{1-b} \qquad \text{and} \qquad b = \beta \tag{17}$$

with the implicit assumption that N_0^* is *constant* along path.

Eq.(14) constitutes an exact solution to the inversion of Eq.(13). Nevertheless, as recognised by their authors, it is mathematically unstable. One of the reason of this instability is the *variability* of N_0^*. This solution has no practical utility without an external constraint to stabilise it. In the following we describe the various solutions that may be used in the different applications of this paper.

An alternate way to formulate the HB54 solution is to express it with respect to the specific attenuation A. Our specific approach to reformulate the solution is the following:

$$A(r) = A(r_0)\frac{Z_a^{\,\beta}(r)}{Z_a^{\,\beta}(r_0) + A(r_0).I(r,r_0)} \tag{18}$$

where: $$I(r,r_0) = 0.46b\int_r^{r_0} Z_a{}^{\beta} ds \tag{19}$$

In (18), the profile of specific attenuation $A(r)$ is expressed as a function of $A(r_0)$ (unknown) at *arbitrary* reference range $r_0 > r$. It is interesting to note that with this formulation, $A(r)$ is independent of the DSD variability (N_0^* is eliminated in this formulation), and independent of the radar calibration. However $A(r_0)$ is introduced as a new unknown and should be determined using the external constraint. Also, since the primary parameter considered in the retrieval is $A(r)$, the rain rate should be further estimated from A, according to our inverse model as:

$$R = c\left[N_0^*\right]^{1-d} A^d \tag{20}$$

3.2. Application to the TRMM precipitation radar

With the TRMM precipitation radar (PR), the external constraint is supplied by the "path integrated attenuation" (PIA) estimated from the surface echo used as a reference target. This expresses as:

$$\int_0^{r_s} A(s)ds = PIA \tag{21}$$

where r_s is the range of the surface.

Considering r_s as the reference range in (18), and after introduction of A given by (18) in (21), it is straightforward to derive the expression of $A(r_s)$ as:

$$A(r_s) = \frac{Z_a{}^{\beta}(r_s)}{I(0,r_s)}\left\{\exp\left[0.46\beta.PIA\right]-1\right\} \tag{22}$$

with:

$$I(0,r_s) = 0.46\beta\int_0^{r_s} Z_a{}^{\beta} ds \tag{23}$$

Moreover, comparing $A(r_s)$ and $Z_e(r_s)$, N_0^* may be estimated as:

$$N_0{}^* = \left[\frac{1}{\alpha}\frac{\left\{1-\exp\left(-0.46\beta.PIA\right)\right\}}{I(0,r_s)}\right]^{\frac{1}{1-\beta}} \tag{24}$$

Profiles $A(r)$ and $R(r)$ may subsequently be determined using (18) and (20).

With the TRMM PR, the accuracy of the estimate of $A(r_s)$ and N_0^* derived from (22) and (24) are subject to the statistical uncertainty and bias in the scattering cross section of the surface σ_0. It is obviously for heavy rain that the algorithm is expected to provide the best results (since the relative uncertainty in PIA will be then minimised. It is also interesting to recall that note that the retrieved $A(r)$ profile [through (18) and (22)] is not subject to radar calibration C (in dB), while N_0^* derived from (24) is deeply subject to C as:

$$\Delta\left[\log_{10}(N_0{}^*)\right] = -\frac{C}{10}\frac{\beta}{1-\beta} \tag{25}$$

It is possible to exploit the statistical stability of the N_0^* histogram to check the calibration of the radar.

3.3. Application to the Darwin C-band polarimetric radar: Algorithm ZPHI

With the Darwin polarimetric radar, the radar observables are the apparent radar reflectivity Z_a, the apparent differential reflectivity Z_{DRa}, the differential phase shift Φ_{DP}, the coherence coefficient ρ_{HV}.

Using the quasi-linear relationship between A and K_{DP} [noted $A = \gamma.K_{DP}$], the path integrated attenuation PIA_{i-1}^{i} between two bounds r_{i-1} and r_i may be estimated from Φ_{DP} as:

$$PIA = \int_{i-1}^{i} A(s)ds = (\gamma/2).\{\Phi_{DP}(r_i) - \Phi_{DP}(r_{i-1})\} \tag{26}$$

As a consequence, the attenuation profile $A(r)$ between the same bounds may be derived from (18) using r_i as the reference range, $A(r_i)$ being given by:

$$A(r_i) = \frac{Z_a{}^{\beta}(r_i)\{\exp[0.23\beta(\Phi_{DP}(r_i) - \Phi_{DP}(r_{i-1}))/\gamma] - 1\}}{I(r_{i-1}, r_i)} \tag{27}$$

Thus, with the polarimetric radar, the analysis may be segmented along the beam, and this segmentation may be optimised in order to take into account that different types of rain (stratiform or convective) may be encountered along the beam with distinct N_0^*s. The N_0^* estimator along each segment is similar to (24), except that it should account for the along attenuation due to the previous segments (see more details in Testud et al, 2000).

Figs. 3 and 4 illustrate results obtained with the Darwin polarimetric radar.

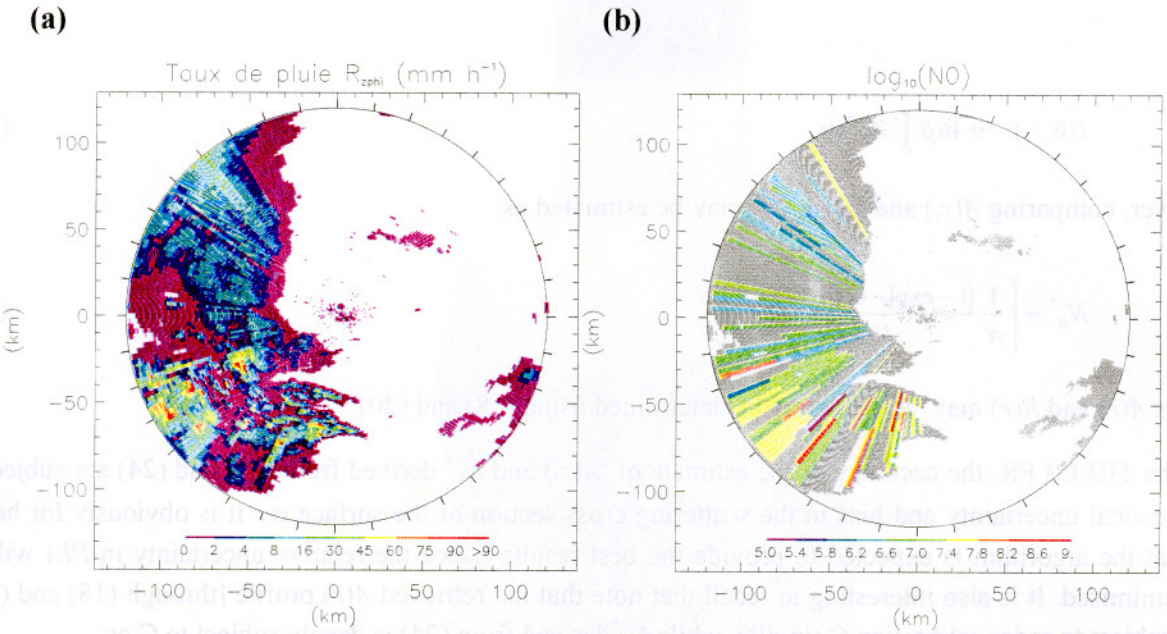

Fig. 3: Conical scan views (at 1.6° elevation, 19 January 1998 around 22:40Z) of : (a) the rainfall rate derived from ZPHI; (b) $\log_{10}(N_0^*)$ retrieved by ZPHI (in gray when forced to the Marshall-Palmer's value.

Fig. 3 displays a PPI at 1.6° elevation and 120 km range with heavy rain convective cells in the SW sector and light stratiform rain in the NW sector (left diagram). The right diagram shows the segmentation with

associated retrieved N_0^*. The values of N_0^* observed in convective [$\log_{10}(N_0^*)$ between 7 and 7.6] and in stratiform [between 6.2 and 6.6] are fully consistent with that expected from the statistics of the Darwin disdrometer or of the TOGA-COARE airborne microphysical data.

There is two calibration techniques that are available from ZPHI. The first in founded upon the stability of the N_0^* histogram: it consists of adjusting the radar calibration in order to bring to coincidence the histogram observed with the ground based disdrometer and that derived by the radar. The second one is purely internal to the radar: the radar calibration is tuned to obtain the best correlation between the current R estimate by ZPHI (funded upon A and N_0^*), and an alternate estimate (funded upon A and Z_{DR}). The two calibration techniques lead a consistent correction of -1 dBZ on the original data.

Fig.4 illustrates a validation of algorithm ZPHI using the Darwin radar and its associated rain gauge network. Radar and rain gauge have quite different time and space resolution, and sampling strategy. The time resolution of the rain gauge network is one minute, and the spacing between rain gauges is typically 10-20 km. The radar operates conical scanning at various elevations with revisit time of 12 minutes. Only the scan at 1.6° elevation is selected for comparison with rain gauges. To compensate for these different sampling characteristics, the radar estimate is averaged (i) in space, within a circle of 2 km radius centred at rain gauge site, and (ii) in time over three scans within ± 15 minutes. The corresponding rain gauge data is averaged over ± 15 minutes.

Fig. 4a is a scatter plot representing a "point-by-point" comparison, covering seven rainy days of January 1998, between the rain rate estimate by ZPHI (noted R_{ZPHI}) and that by the rain gauges (G). For reference, Fig. 4c displays the same scatter plot, but with the "classical" estimate $R(Z_a)$ [Standard Z-R relationship without consideration of along path attenuation]. Fig.4b shows the same scatter plot, but with an estimate noted $R(A)$ based on the retrieved attenuation only, at fixed N_0^*.

Fig. 4c confirms that the classical estimate is severely biased with respect to the rain gauge one: the slope of the linear correlation is 0.37 (which means that as average, the classical estimate $R(Z_a)$ is only 37% of the gauge estimate G). The use of the $R(A)$ estimate with fixed Marshall-Palmer N_0^* sensibly reduces the bias. The slope increases to 0.58, which is a serious improvement with respect to the "classical estimate". With the R_{ZPHI} estimate (where the $R(A)$ relationship is tuned for the retrieved N_0^*) the slope jumps to 0.84. This demonstrates that not only the correction for attenuation, but also the N_0^* adjustment, is critical to retrieve good rainfall rate estimate at C-band. Another important statistical feature is the regular improvement of the "linear correlation coefficient" from Fig. 4c to Fig. 4a: ρ=0.871 with the classical estimate; ρ=0.904 with the $R(A)$ estimate with fixed N_0^* ; ρ=0.918 with R_{ZPHI}.

3.4. Airborne dual beam Doppler Radar

The concept of dual beam airborne Doppler radar have been invented to deploy the equivalent of a dual Doppler ground based radar experiment, over unreachable regions like open ocean or mountainous areas. The principle is illustrated in Fig.10: the antenna system mounted in the aircraft tail, rotates about a horizontal axis collinear to the aircraft fuselage. The radar feeds two antennas mounted back to back, one looking 20° fore and the other 20° aft. The antenna rotation associated to the aircraft motion produces a dual helical scan (Fig.10) allowing to sample any point of the three dimensional space along *two viewing angles*. The time shift between the "fore" and "aft" samplings (typically 2 minutes at 20 km range) is moderate enough with respect to the characteristic evolution time of a storm (typically 20 minutes), in order to allow one considering a "quasi stationary" hypothesis in the data processing.

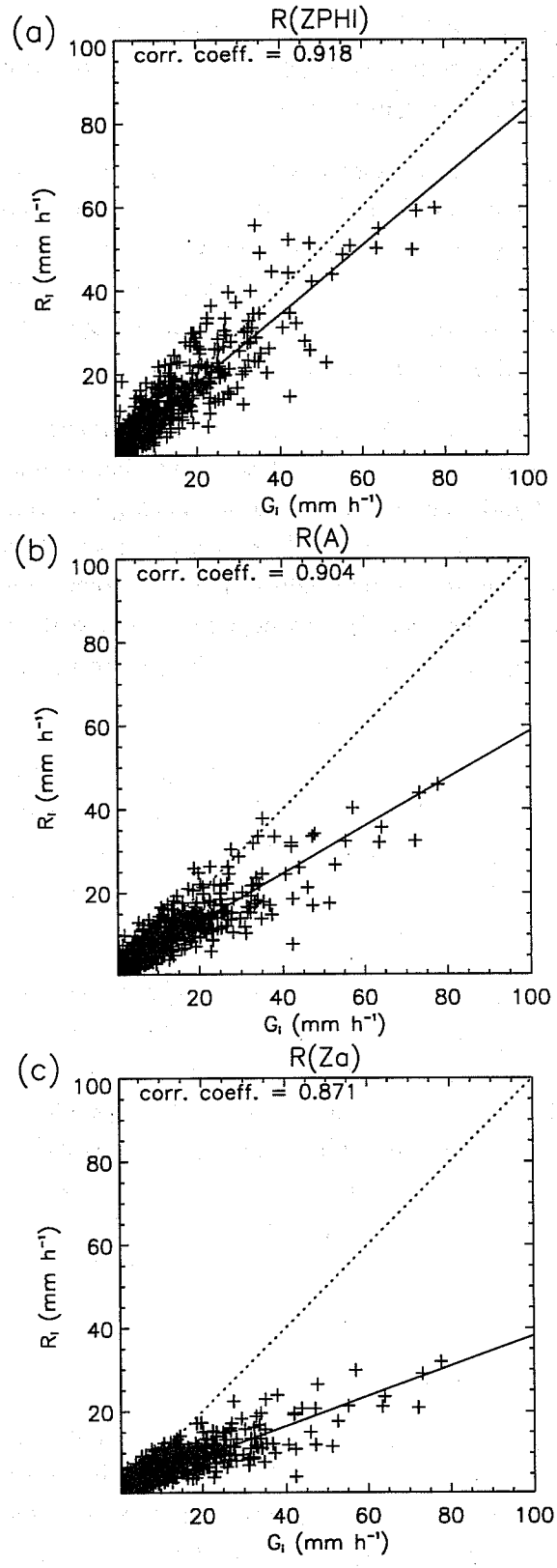

Fig. 4 : "Point by Point" comparison, during seven days of January 1998, of gauge rainfall rate G, with collocated radar-derived estimates: (a) current ZPHI estimate, (b) R-A relation with fixed N_0, (c) classical" estimate R-Z_a. The rain gauge data are averaged over ± 15 mn, and the radar data are averaged over ±mn and within a circle of 2 km radius about the rain gauge.

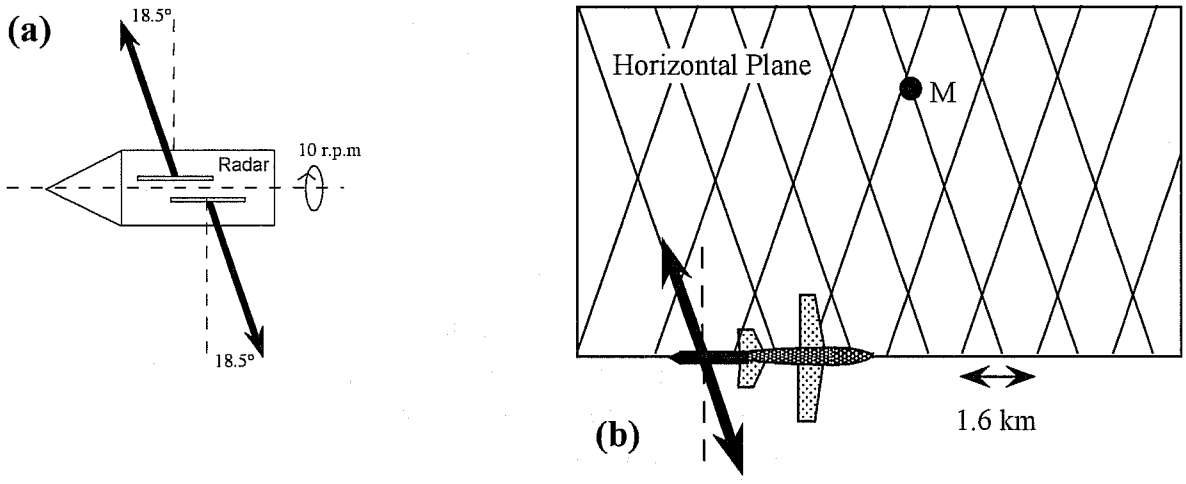

Fig. 5: Principle of the dual beam airborne Doppler radar. (a) the antenna system is rotating about an horizontal axis collinear to the fuselage, one antenna is looking fore and the other aft. (b) Owing to the aircraft motion, a dual helical scan is obtained. Each point of the three-dimensional space is sampled successively by the fore an the aft antenna, with a time shift of about 2 minutes at 20 km range.

Dual beam (or pseudo-dual beam) radars have been the object of joint development by NOAA and CETP one the one hand, and by NCAR and CETP on the other hand. The first pseudo-dual beam airborne Doppler radar experiment was accomplished in July 1989 in Florida during CAPE, with the NOAA-P3 tail radar equipped with a dual beam antenna of CETP. The ELDORA-ASTRAIA radar jointly developed by NCAR and CETP and mounted on the NCAR Electra [see description in Hildebrand et al., 1994], flew for the first time in TOGA-COARE (November 1992- February 1993). The radar used in the present study is the original NOAA system operated according to the FAST methodology (Forward and Aft Scanning Technique, Jorgensen et al., 1996).

The three-dimensional wind field synthesis from dual Doppler radar data, is very similar with a ground based radar experiment and with the airborne radar. The retrieval should be constrained with the air mass continuity equation (expressed under its anelastic form), with special attention to the boundary condition. These techniques are now well dominated and will not be reviewed in this paper. For details the reader is referred to Testud and Chong (1983), Chong et al. (1983), Chong and Testud (1983, 1996), Scialom and Lemaître (1990), Protat et al (1998).

The above mentioned airborne radars operate at X-band. The choice of this frequency is a trade-off between antenna size and beam resolution. However at X-band, the along path attenuation may be quite severe through heavy rain, and the correction of the « apparent » reflectivity for attenuation is a key issue to obtain a satisfactory rain rate retrieval. Two algorithms were developed at CETP for that purpose, called "stereoradar" and "dual beam". Both take advantage of the two viewing angles authorised by the dual beam scanning strategy.

The "dual beam" algorithm is an integral algorithm of the same family as the above algorithms for the TRMM PR for the Darwin C-POL radar [see description in Testud et Oury, 1997 or in Oury et al. (2000)]. The starting point is to assume that N_0^* is uniform within the particular convective cell of interest, that is, along the two paths corresponding to the two viewing angles. Then one applies the HB54 algorithm along the two beams and one expresses that the two corrected reflectivities should be the same. This helps to estimate N_0^*, and to further derive a "corrected" Z and R not any more subject to algorithm instability or DSD variability. The drawback of the dual beam algorithm is that it collapses when the path integrated attenuations from the two viewing angles are equal, which generally happens at the very centre of the raincell.

The "stereoradar algorithm", developed by Kabèche and Testud (1995), is a differential algorithm that does not require *any hypothesis* on the type of hydrometeor nor on the *A-Z* relationship. But it has some drawbacks with respect to the dual beam algorithm: it is much more noisy, and it requires boundary conditions sometimes difficult to meet. The "hybrid" algorithm developed by Oury et al. (2000) couples the dual beam and the stereoradar algorithms. It uses the dual beam algorithm to generate the boundary conditions needed for the stereoradar algorithm. With this strategy, the hybrid algorithm is much more flexible than the stereoradar or the dual beam alone. Thus, the hybrid algorithm is particularly indicated when an extensive application to a large data set is anticipated, as in the present study.

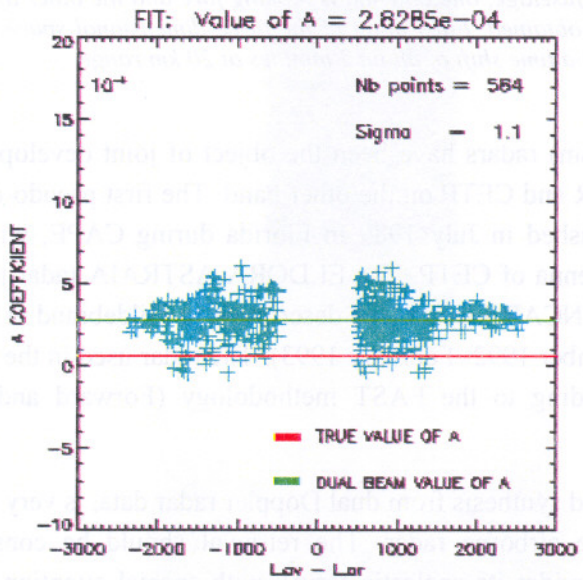

Fig. 6: Comparison between the a coefficient of the $A=aZ^b$ relationship, derived from the microphysics (in red) and the one estimated from the dual beam data in Bonnie (in green). The difference is interpreted as a radar under calibation of $-(10/b)\log(a_{red}/a_{green}) = -7.3$ dB.

A major interest of the dual beam algorithm is to provide an approach to calibrate the radar independently of any technical measurement. The primary product of the dual beam algorithm is an estimate of the *a* coefficient of the relationship $A = aZ^b$ [see Eqs. 16 and 17]. But this *a* estimate is subject to radar calibration. The *a* coefficient may be estimated independently from processing the microphysical data [available on the NOOA-P3 that flew in CAMEX]. By comparison of the two estimates, a quite accurate calibration of the radar may be performed (illustrated in Fig. 6). For CAMEX it was found that the NOAA-P3 tail radar was under calibrated by 7.3 dB.

Fig. 7 illustrates an application of the hybrid algorithm to hurricane Georges observed by the NOAA P3-42 aircraft on 19 September 1998. It is seen that the hybrid algorithm performs a quite substantial correction with respect the "max reflectivity between the fore and the aft looks " currently used by many authors to mitigate the effect of attenuation.

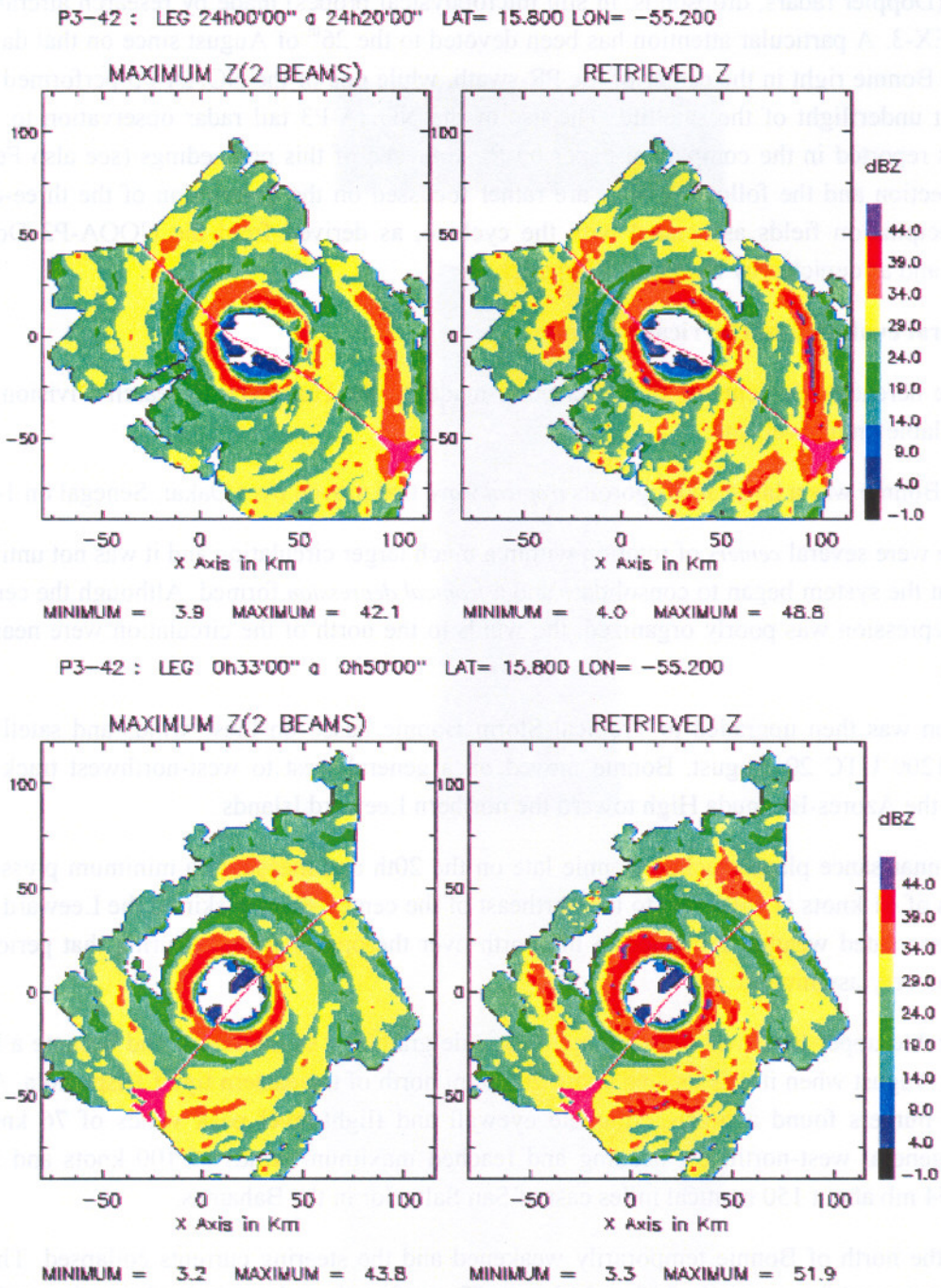

Fig.7: Reflectivity fields at 3.2 km altitude derived from two legs of the P3-42 aircraft throw hurricane Georges (on 19 September 1998). Left diagrams display the max reflectivity between the fore and the aft looks, and the right diagrams, the application of the hybrid algorithm.

4. Observations of hurricane Bonnie during CAMEX

In the framework of EuroTRMM, the first 15-day period that was selected for the experiment of assimilation of the TRMM data in the ECMWF model, was 15-30 August 1998. This period covers the full life time of Hurricane Bonnie in the Mexico Gulf, that was particularly well documented by various types of observations (Doppler radars, dropsonds, in situ microphysical probes) made by research aircrafts deployed within CAMEX-3. A particular attention has been devoted to the 26th of August since on that day, a TRMM pass captured Bonnie right in the center of the PR swath, while one of the NOAA-P3 performed at the same time a perfect underflight of the satellite. The use of the NOAA-P3 tail radar observation to validate the TRMM-PR is reported in the companion paper by P. Amayenc of this proceedings (see also Ferreira et al. 2000). This section and the following ones are rather focussed on the description of the three-dimensional wind and precipitation fields associated with the cyclone, as derived from the NOOA-P3 Doppler radar observations, and as depicted by the ECMWF model.

4.1. General evolution of Hurricane Bonnie

We reproduce hereafter elements of the description made by the Hurricane Research Division of NOAA-ERL and available on his web site:

The origin of Bonnie was a large and vigorous *tropical wave* that moved over Dakar, Senegal on 14 August..

Initially, there were several *centers* of rotation within a much larger circulation and it was not until 1200 UTC 19 August that the system began to consolidate and a *tropical depression* formed. Although the central area of the tropical depression was poorly organized, the winds to the north of the circulation were nearing *tropical storm* strength..

The depression was then upgraded to Tropical Storm Bonnie based on these winds and satellite intensity estimates at 1200 UTC 20 August. Bonnie moved on a general west to west-northwest track around the circulation of the Azores-Bermuda High toward the northern Leeward Islands..

The first reconnaissance plane reached Bonnie late on the 20th and measured a minimum pressure of 1004 mb and winds of 61 knots at 1500 feet to the northeast of the center. Bonnie skirted the Leeward Islands and most of the associated weather remained to the north over the open Atlantic. During that period, Bonnie's circulation was very asymmetric..

Under a favorable upper-level wind environment, Bonnie gradually strengthened and became a hurricane at 0600 UTC 22 August when it was located about 200 n mi north of the eastern tip of Hispaniola. At that time, the hurricane hunters found a nearly complete eyewall and flight-level peak winds of 76 knots. Bonnie moved on a general west-northwest heading and reached maximum winds of 100 knots and a minimum pressure of 954 mb about 150 nautical miles east of San Salvador in the Bahamas.

The ridge to the north of Bonnie temporarily weakened and the steering currents collapsed. The hurricane then drifted northward for a period of 18 to 24 hours. Thereafter, the subtropical ridge re-intensified, forcing Bonnie to move northwestward and then northward toward the coast of North Carolina while the hurricane maintained winds of 100 knots.

After a slight weakening, the eye of Bonnie passed just east of Cape Fear around 2130 UTC 26 August and then made landfall near Wilmington as a border line Category 2/3 hurricane on the Saffir/Simpson Hurricane Scale (SSHS) around 0330 UTC 27 August.

The evolution of the minimum central pressure of Hurricane Bonnie between August 19th and 30th, 1998 is given in Fig. 8. Several missions of the NOAA-P3 aircrafts investigated the storm center during this period. As said before, in this paper we will focus on the mission of the NOAA-P3-42 on August 26th between 1136Z and 1705Z. On this day the TRMM pass is around 1137Z. With respect to storm evolution, this mission covers the mature stage of the storm, just before the decaying phase, as attested by Fig. 8.

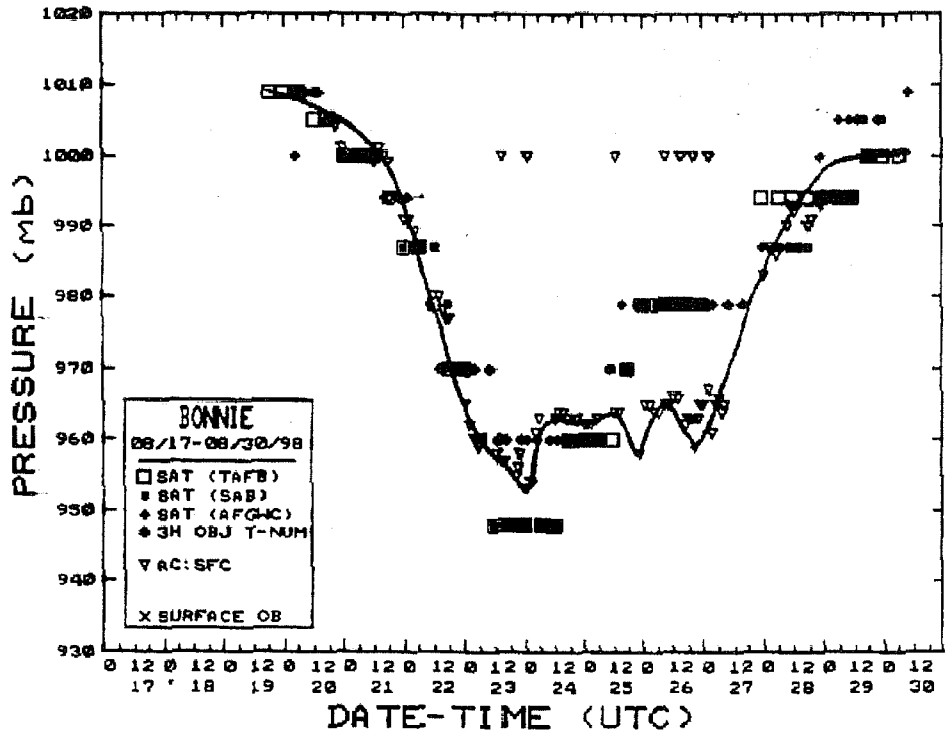

Best track minimum central pressure curve for Hurricane Bonnie.

Fig. 8: Best track minimum central pressure for hurricane Bonnie between 19 and 30 August 1998

4.2. Reflectivity and rain rate retrieval from the NOAA-P3 tail radar

The objective of the reflectivity and rain rate retrieval is twofold:

(i) to provide carefully corrected and navigated R and Z data that will serve as ground truth for the TRMM over pass;

(ii) to provide a general picture of the precipitation field at the space and time scale of the hurricane dynamics.

For the first objective it is essential to take account of the advection velocity of individual convective cells in the application of the hybrid algorithm. In the hurricane environment, there is two components in the advection velocity of a convective cell. The first one is associated to the hurricane motion as a whole. It may be assimilated to a translation velocity along storm track (and will be referred to, in the following as "translation velocity"). The second is a rotation velocity around hurricane center. This "rotation velocity" may be estimated by tracking each individual cell motion from the lower fuselage C-band radar of the P3.

Fig. 9 displays the "rotation velocity" (in m/s) determined from this technique using an HRD (Hurricane Research Division) software package. The maximum rotation velocity is obtained at a distance from the center of ≅ 27 km and reaches 40 m/s.

Fig. 10 illustrates the application of the hybrid algorithm combined with the advection scheme appropriate for individual cells. The selected P3-42 leg [1136Z to 1219Z] is that corresponding to the TRMM underflight. The reference time for the advection scheme is 1137Z, the best coincident time between the airborne and spaceborne samplings. The TRMM reflectivity field (before and after correction of attenuation) is also shown in Fig. 9. The reflectivity fields from airborne and from space are in good agreement, especially in the area where the time coincidence is within ± 7.5 mn. This comparison is discussed in more details by P. Amayenc in a separate paper of this proceedings. The intense rain band depicted by the TRMM 2A25 algorithm in the NW sector of the hurricane is hardly seen by the P3-42 tail radar because of a total extinction of the signal (as a result of the combined effect of range and along path attenuation).

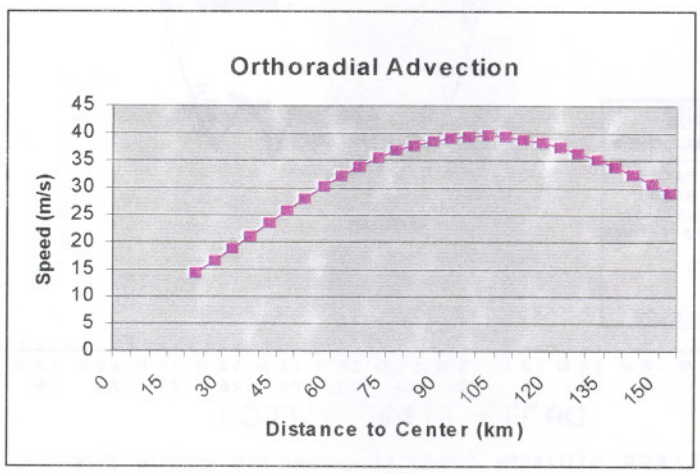

Fig.9: Rotation velocity of the rain cells versus distance to storm centre (determined from tracking the individual cell motion from the lower fuselage C band radar).

For the second objective, to derive a general picture of the precipitation field associated with the hurricane, it is not appropriate to correct for "rotation velocity" of individual cells. To sample the hurricane as a whole, the aircraft flies along two "figure 4" patterns (see Fig.11), which takes about 5 hours. Meanwhile the life time of a convective cell is typically 20 mn. Thus that would not make sense to advect a convective cell for 5 hours. Moreover, the underlying hypothesis of an analysis of the "full" flight (using the 5 hour sampling) is that the dynamics of the hurricane evolves with a characteristic time larger than 5 hours, allowing to consider the mesoscale airflow to be "quasi stationary" within the sampling time (in the reference frame in translation with the hurricane). Embedded in the mesocale airflow, the convective cells preferentially initiate and grow when the environment is more unstable and decay where it is less unstable. Advecting the cells for 5 hours (e.g. 700 km at the rotation velocity of 40m/s) would give a totally misleading picture, bringing artificially convection where there should not be some.

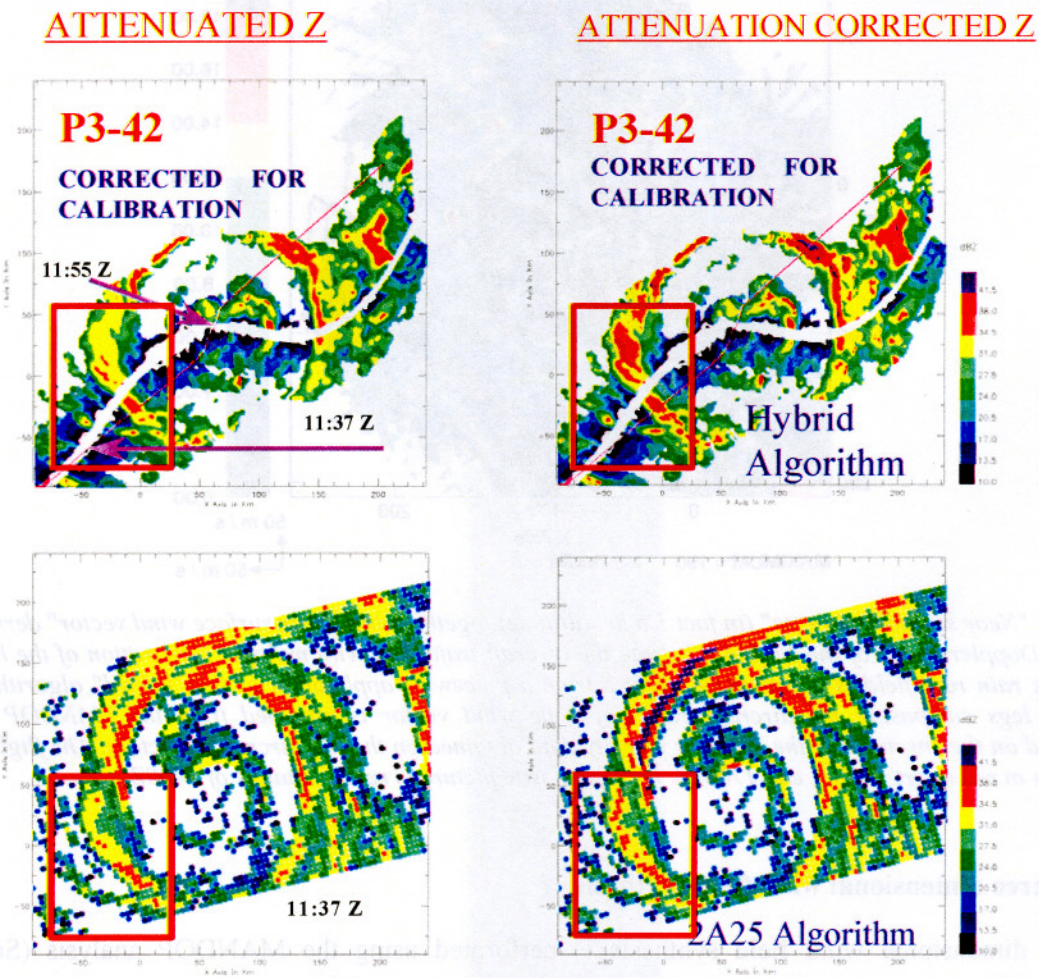

Fig. 10. TRMM observation of Bonnie and NOAA/P3-42 under flight. ***Upper diagrams****: X-band reflectivity field retrieved from the P3- 42 tail radar, after calibration and correction for advection (including translation and rotation); left diagram without correction for attenuation; right diagram with correction for attenuation by the "hybrid algorithm".* ***Lower diagrams****: Ku band reflectivity field observed by TRMM without (left diagram) and with (right diagram) correction for attenuation (TRMM products).* The reference time *for advection correction is time of TRMM pass: 1137Z. Within the red rectangle, the time shift between the TRMM and P3-42 samplings is within ± 7.5 mn.*

Fig. 11 displays a composite picture of the rain rate field at the hurricane scale, built from assembling the fields derived from the various legs composing the flight. The hybrid algorithm is applied for each leg without consideration of the rotation velocity in the advection scheme. From this picture the eyewall marked by enhanced convection is at 80 km from hurricane center.

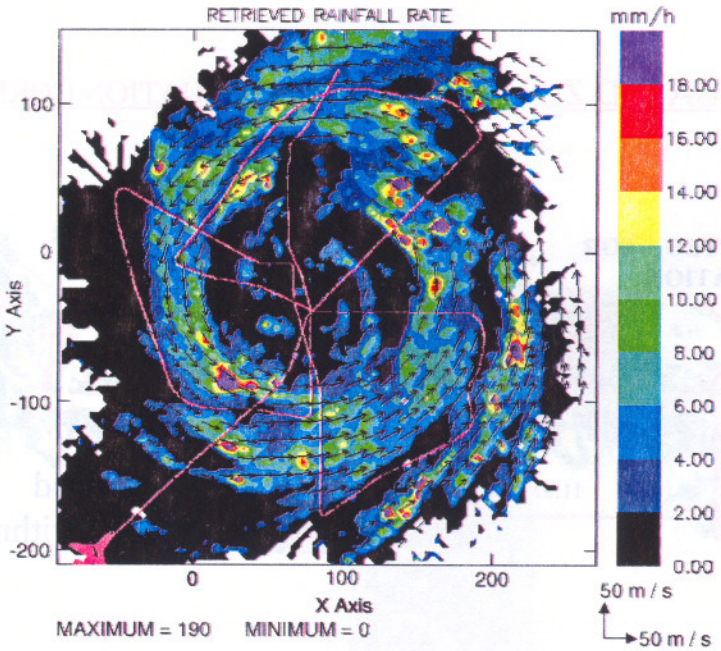

Fig. 11: *"Near surface rain rate" (in fact 1.6 km altitude) together with "near surface wind vector" derived from the tail Doppler radar of the NOOA-P3. Note the aircraft trajectory with multiple penetration of the hurricane eye. The rain rate field is a composite picture from a piecewise application of the "hybrid" algorithm to the various legs composing the aircraft trajectory. The wind vector is obtained from the MANDOP analysis practised on the ensemble of the Doppler velocity data obtained on the full aircraft trajectory. The flight pattern is shown in red (start 1136Z; end 1705Z). This composite picture is representative of 1400Z.*

4.3. Three dimensional wind field synthesis

The three dimensional wind field synthesis is performed using the MANDOP analysis (Scialom and Lemaître, 1990; Protat et al., 1998) consisting of adjusting the coefficients of an analytical expansion of the three-dimensional wind field to best represent the radial velocity data set. Presently the data set of the full flight - 5 hours long - is considered as a whole, with the underlying hypothesis previously mentioned that the airflow is quasi stationary at this time scale. The space domain considered covers 350x350 km^2 horizontally and 15 km vertically, with a grid resolution of 3x3 km^2 horizontally and 0.4 km vertically. Nevertheless, the scales that the analysis may resolve are defined by the ratio of the size of the domain (350 km) to the order of the development, chosen to 5 in the present analysis. In the present application, it is estimated that the lowest scale resolved in about 40 km, which just fits the resolution of the ECMWF grid with T511 truncation.

Figs. 12 and 13 illustrate the three dimensional airflow associated with the hurricane. These patterns are representative of the airflow at mid-flight time, e.g. 1400Z. Fig. 12 shows the horizontal wind vector at 1.6 km altitude together with a colour display of the corresponding wind speed. Fig. 13 compares the same horizontal wind vector at 1.6 km with the vertical velocity at 3 km altitude.

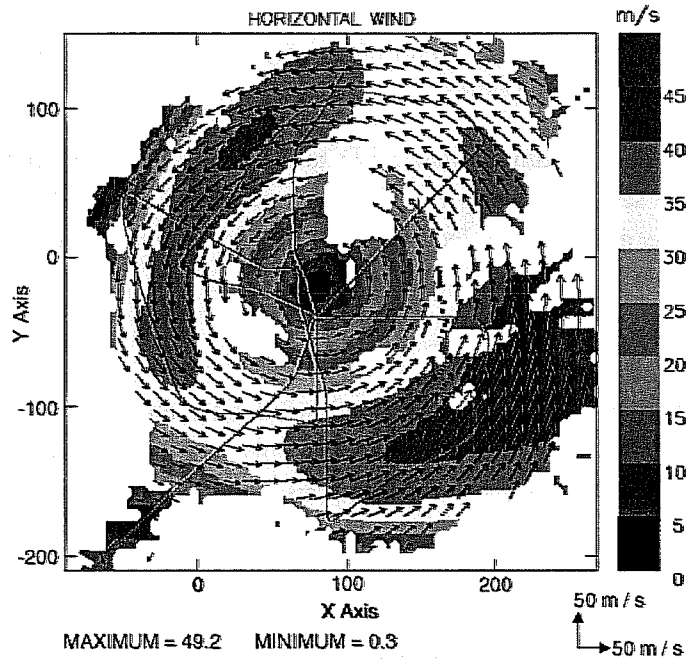

Fig. 12: As Fig. 11, but comparing "near surface" (1.6 km altitude) wind intensity (see colour code) and wind vector.

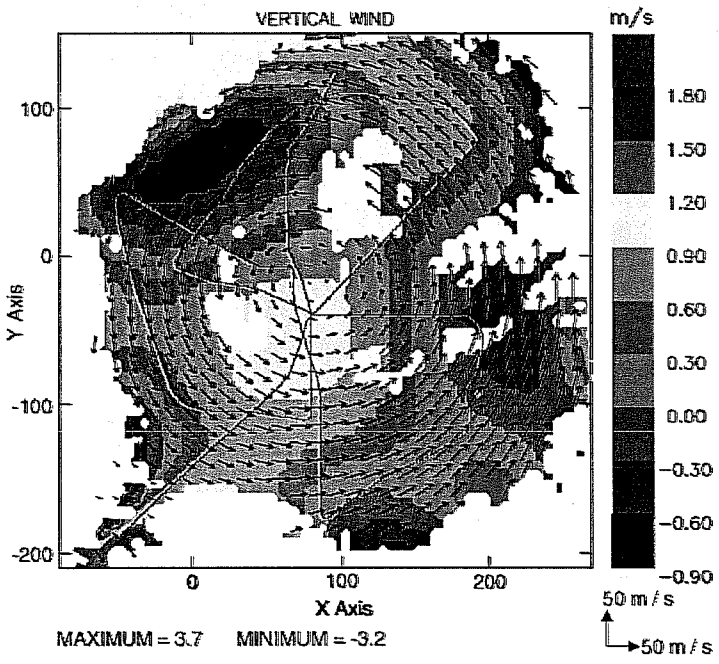

Fig. 13: As Fig. 11, but comparing the mesoscale vertical velocity at 3.2 km altitude (see colour code) and "near surface" (1.6 km altitude) wind vector.

The "near surface" horizontal airflow shows an asymmetry characterised by two regions of acceleration: the first one in the NW at about 120 km distance from centre, and the second in the ESE sector at about 150 km from centre. These regions of low level acceleration appear collocated with mesoscale downdrafts at 3 km altitude. The downdraft reaches -70 cm/s in the NW sector and – 50cm/s in the ESE sector. Correlatively updrafts are observed at 3 km altitude in the SW sector and NE sectors. The storm centre appears as a region of updraft, but this could be an artefact of the wind field synthesis due to the fact that numerous flight tracks with important time shift intersects in this limited area (which may affect the divergence estimate).

The collocation between mesoscale downdrafts and low level acceleration of the flow deserves more investigation: how frequent is this type of feature in hurricanes? is there a particular role of the cooling by evaporation in the dynamics of accelerated flow?

The uncertainty associated to the three dimensional field analysis also deserves more attention. The sampling time of the radial velocity data set is not evenly distributed in space and time, but is a deterministic function of the flight pattern. How the analysis is affected by the hurricane evolution within the sampling time remains to be evaluated.

4.4. Comparison with the ECMWF model

The comparison of the present P3-42 three dimensional wind field analysis with an ECMWF output is necessarily limited because, at the scale of the model, it is only a snapshot in time, and it covers a quite limited area in space (as illustrated in Fig. 14). At most can we may compare some broad features of the flow.

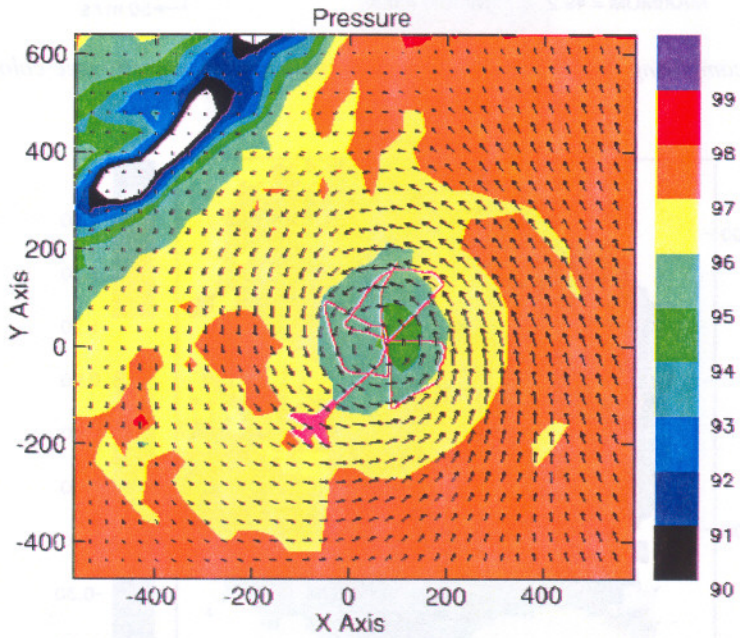

Fig. 14: *The environment of Hurricane Bonnie as depicted by the ECMWF model on August 26th at 12:00Z. The centre of rotation of the cyclone taken as reference in the following, is at, (+80, –10).*

Figs. 15 and 16 illustrate a forecast of the ECMWF model on 26th August 1998 at 12.00Z, based on an analysis on 25th August 1998 at 1800Z in which the "EuroTRMM rain product" is assimilated. The space domain represented in these two figures is centred over hurricane centre and has the same size as that of Figs 12 and 13. Fig. 15 represents the horizontal wind vector à 1.6 km together with the wind speed at the same level (as Fig. 12). Fig.13 compares the horizontal wind vector at 1.6 km with the vertical velocity at 3.2 km. Concerning the horizontal wind at 1.6 km, the asymmetric pattern produced by the model is quite similar to that of the observation. The regions of flow acceleration are in the same sectors: NW at about 200 km from storm centre, and East at 200km from storm centre. The horizontal wind intensity is slightly reduced (by 5to10 m/s) with respect to P3-42 observation in accordance with an increased size of the ring of maximum wind speed.

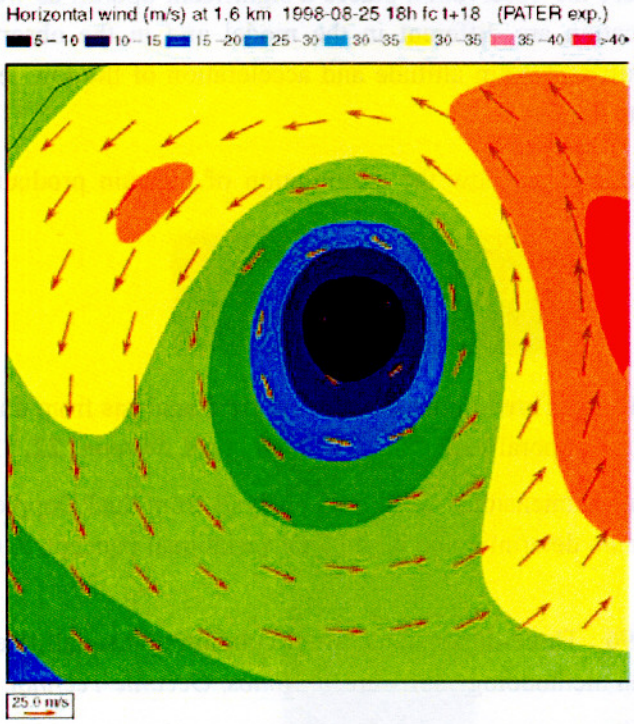

Fig. 15. *Horizontal wind intensity (color code) and horizontal wind vector at 1.6 km altitude produced by the ECMWF model at the resolution 0.36°x0.36°: forecast on 26th August 1998 at 12.00Z, from an analysis on 25th August 1998 at 1800Z with assimilation of the "EuroTRMM product" (calibration of TMI by PR).*

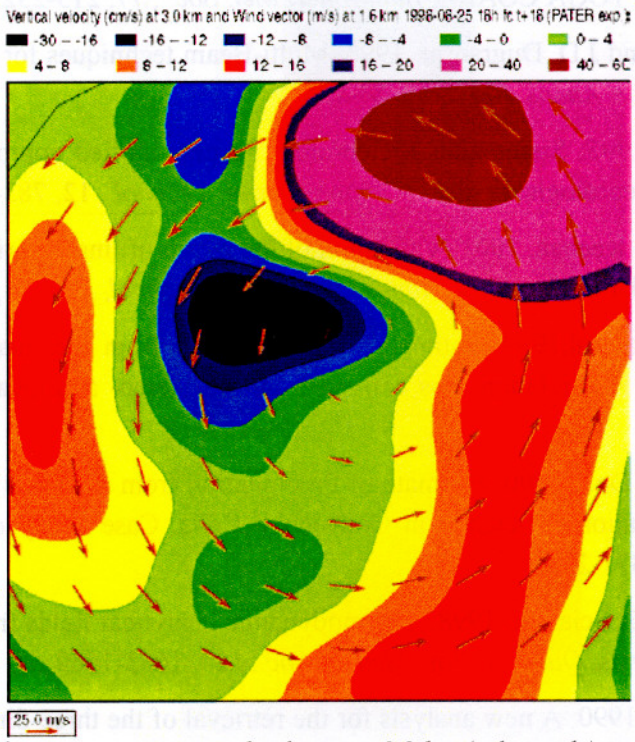

Fig. 16: *Same as Fig. 15, but comparing vertical velocity at 3.2 km (color code) and horizontal wind vector at 1.6 km altitude.*

Concerning the vertical velocity at 3.2 km altitude, a relatively intense mesoscale updraft is produced by the model in the NNE sector where the observation places a significant updraft as well. But the morphology of the downdrafts and their location are different in the model and in the observation. Also the apparent relationship between downdraft at 3.2 km altitude and acceleration of the low level horizontal flow seems less apparent in the model output.

More analysis is needed to appreciate how the assimilation of the rain product affects and modifies the dynamics of the cyclone.

References

Chong, M., J. Testud, and F. Roux, Three-dimensional wind field analysis from dual Doppler radar data. Part II - Minimizing the error due to temporal variation, *J. Climate Appl. Meteor.*, **22,** 1216-1226, 1983.

Chong, M., and J. Testud, Three-dimensional wind field analysis from dual Doppler radar data. Part III - The boundary condition : an optimum determination based on a variational concept, *J. Climate Appl. Meteor.*, **22**, 1227-1241, 1983.

Chong, M., and J. Testud, 1996 : Three-dimensional air circulation in a squall line from airborne dual-beam Doppler radar : a test of coplan methodology software, *J. Atmos. Oceanic Technol.* **13**, 36-53, 1996.

F. Ferreira, P. Amayenc, S. Oury, and J. Testud, 2001 : Study and Tests of Improved Rain Estimates from the TRMM Precipitation Radar , *J. Appl. Meteor* (in press).

Hildebrand, P.H., W.-C. Lee, C.A. Walther, C. Frush, M. Randall, E. Loew, R. Neitzel, R. Parsons, J. Testud, F. Baudin, and A. Le Cornec, 1996 : The ELDORA/ASTRAIA airborne Doppler weather radar: Design and Observation from TOGA COARE, *Bull. Amer. Met. Soc.* , **77**, 213-232.

Jorgensen D.P., T. Matejka and J.D. Dugranrut, 1996: Multi-Beam techniques for deriving wind fields from airborne Doppler radar. *Meteor. Atmos. Phys.*, **59**, 83-104

Kabèche A. and J. Testud, 1995: Stereoradar Meteorology: a new unified approach to process data from airborne or ground-based meteorological radar. *J. Atmos. Ocean. Technol.*, **12**, 783-799.

Le Bouar E., J. Testud and T. Keenan, 2001: Validation of the rain profiling algorithm " ZPHI " from the C-band polarimetric weather radar in Darwin. *J. Atmos. and Ocean, Technol, Dec. In press.*

Oury S., J. Testud et V. Marécal,1999: Estimate of precipitation from the dual beam airborne radar in TOGA-COARE. Part 1: The K-Z relationships derived from the Stereo- and Quad beam analysis. *J. Appl. Meteor.*, **38**, 156-174.

Oury S., J. Testud and X.-K. Dou, 2000: Estimate of Precipitation from the Dual Beam Airborne Radars in Toga-Coare. Part 2: Precipitation Efficiency in Convective Cells. Case Study of 9Th. February 1993, *J. Atmos. Ocean.Technol.* **39,** 2371-2384.

Protat, A., Y. Lemaître, and G. Scialom, 1998: Thermodynamic analytical fields from Doppler radar data by means of the MANDOP analysis. *Quart. J. Roy. Meteor. Soc.*, **124**, 1633-1669.

Scialom G. and Y. Lemaître, 1990: A new analysis for the retrieval of the three-dimensional wind field from multiple Doppler radars, *J. Atmos. Ocean. Technol.*, **7**, 640-665.

Testud, J., and M. Chong, 1983: Three-dimensional wind field analysis from dual Doppler radar data. Part I - Filtering, interpolating, and differentiating the raw data, *J. Climate Appl. Meteor.*, **22**, 1204-1215.

Testud J. and S. Oury, 1997: Algorithme de correction d'atténuation pour radar météorologique, *C. R. Acad. Sc. Paris, t324*, Série 2a, 705-710

Testud J., E. Le Bouar, E. Obligis, M. Ali Mehenni, 2000: The rain profiling algorithm applied to polarimetric weather radar, *J. Atmos. Ocean. Technol.*, **17**, 332-356.

Testud J., S. Oury, P. Amayenc and R. Black, 2001: The concept of "normalized" distribution to describe raindrop spectra: a tool for cloud physics and cloud remote sensing, *J. Appl. Meteor.*, **40**, 1118-1140.